Catalysis Science & Technology

ROYAL SOCIETY OF CHEMISTRY

PAPER

View Article Online
View Journal | View Issue

Cite this: *Catal. Sci. Technol.*, 2026, 16, 2807

Disentangling an extended network of Rh complexes in supported ionic liquid phase (SILP) catalysts for hydroformylation: a combined *in situ* IRAS and DFT study

Kailun Zhang,[a] Sophie Mayer,[b] Sharmin Khan Antara,[c] Arsha Cherian,[d] Huiyi Xu,[a] Ana-Sunčana Smith,[de] Nicolas Vogel,[b] Marco Haumann,[cf] Christian R. Wick *[d] and Tanja Retzer *[a]

Ionic liquids (ILs) serve as highly effective thin-film coatings in supported ionic liquid phase (SILP) systems, combining the molecular definition and high activity of homogeneous catalysts with the facile product recovery and recyclability inherent in heterogeneous catalysts. This study investigates a SILP system composed of acetylacetonato(dicarbonyl)rhodium(I) [Rh(acac)(CO)$_2$], 4,5-bis(diphenylphosphino)-9,9-dimethyl-xanthene (xantphos, xp), 1-butyl-3-methylimidazolium bis(trifluoromethylsulfonyl)imide [C$_4$C$_1$Im][NTf$_2$], and SiO$_2$, which is active towards the hydroformylation of ethylene. We employ *in situ* infrared (IR) spectroscopy and density functional theory (DFT) to analyze the interactions among the Rh complex, the xantphos ligand, the IL, and the reactants (H$_2$/CO). Surface-modified SILP wafers with improved reflectivity and wettability allow for successful IR spectroscopic studies in reflection absorption mode. We identify an extended network of Rh species in the SILP system including [Rh(acac)(CO)(xp)], [Rh(acac)(CO)$_2$(xp)] along with the expected hydride derivatives that form in the presence of a reactive gas atmosphere, and show that the IL itself can actively coordinate under the reaction conditions and participate in formation of key intermediates. Among others, the anion can stabilize species such as [HRh(NTf$_2$)(CO)(xp)]$^-$ and the cation might form NHC-based derivatives, such as [Rh(CO)(nhc)(xp)]$^+$, which form at higher temperatures and might persist during cooling.

Received 27th October 2025,
Accepted 9th March 2026

DOI: 10.1039/d5cy01282a

rsc.li/catalysis

1. Introduction

For decades, ionic liquids (ILs) have been used as thin film coatings in various catalytic applications. The supported ionic liquid phase (SILP) concept, introduced by Mehnert *et al.*[1] and Riisager *et al.*,[2,3] involves dissolving a catalytically active transition metal complex in the IL, which is then immobilized as a thin film on an (oxidic) support with a large surface area. This approach combines the benefits of homogeneous catalysts, such as molecular control and high activity, with those of heterogeneous catalysts, including easy product recovery and recyclability of the catalyst.[4,5]

In this context, ILs offer several advantages over traditional solvents such as water[6,7] and/or organic solvents.[8,9] They show negligible vapor pressure and high thermal stability, making them suitable for commercial gas-phase reactions. Additionally, their solvent properties can be tailored through molecular design and a wide variety of possible anion/cation combinations.[10,11] A notable application of SILP systems in (commercial) catalysis is in hydroformylation (see eqn (1)), especially with Rh-based precursors such as [Rh(acac)(CO)$_2$], which are often combined with (bidentate) phosphine ligands (P$_2$), and SiO$_2$ supports.[5]

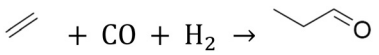

(1)

We recently demonstrated that the IL phase directly affects the catalytic performance of a SILP system. Under hydrogenation conditions, the IL stabilizes the molecular catalyst complexes, inhibiting decomposition.[12] In catalysts

[a] *Interface Research and Catalysis, ECRC, Friedrich-Alexander-Universität Erlangen-Nürnberg, Egerlandstraße 3, 91058 Erlangen, Germany. E-mail: tanja.retzer@fau.de*
[b] *Institute of Interfaces and Particle Technology, Friedrich-Alexander-Universität Erlangen-Nürnberg, Cauerstraße 4, 91058 Erlangen, Germany*
[c] *Lehrstuhl für Chemische Reaktionstechnik, Friedrich-Alexander-Universität Erlangen-Nürnberg, Egerlandstraße 3, 91058 Erlangen, Germany*
[d] *PULS Group and Computational Advanced Materials and Processes (CAMP), Friedrich-Alexander-Universität Erlangen-Nürnberg, IZNF, Erlangen 91058, Germany. E-mail: christian.wick@fau.de*
[e] *Group for Computational Life Sciences, Division of Physical Chemistry, Ruđer Bošković Institute, Zagreb 10000, Croatia*
[f] *Research Centre for Synthesis and Catalysis, Department of Chemistry, University of Johannesburg, P.O. Box 524, Auckland Park 2006, South Africa*

optimized for the water gas shift reaction, the IL phase modifies the speciation of a (freshly prepared) SILP through ligand exchange reactions[13] and enhances catalytic activity by stabilizing transition states *via* intermolecular interactions.[14]

To observe and understand such effects, it is crucial to employ *in situ* or *operando* techniques that provide high sensitivity to changes in the ligand sphere of the transition metal complex. In this context, the investigation of SILP systems using infrared reflection absorption spectroscopy (IRAS) offers clear advantages over the conventional diffuse reflection mode (DRIFTS). Moreover, IRAS is capable to reveal orientation effects[15–17] and reduce gas phase bands through polarization modulation. In order to use this technique, it is however essential to prepare the SILP systems on a flat and highly reflective metal surface.

In this work, we explore a SILP system based on acetylacetonato(dicarbonyl)rhodium(I) $[Rh(acac)(CO)_2]$, 4,5-bis(diphenylphosphino)-9,9-dimethyl-xanthene (xantphos, xp), 1-butyl-3-methylimidazolium bis(trifluoromethylsulfonyl) imide $[C_4C_1Im][NTf_2]$, and SiO_2 that is active towards ethylene hydroformylation. Importantly, this system has been previously shown to be resistant to the formation of nanoparticles from the molecular Rh complex, which is due to the stabilization of the molecular complex by the xantphos ligand.[12] We combine IR spectroscopy in transmission (TIRS) and IRAS mode with density function theory (DFT) calculations and identify the most prominent Rh complexes at different SILP compositions and varying experimental conditions. To accurately perform the experiments, we develop special SILP wafers for temperature-dependent IRAS measurements, which ensure good reflectivity and prevent dewetting of the IL films, thus leading to spectral stability during heating.

With this approach, we study the speciation in the as-prepared SILP catalyst in detail and monitor the formation of the catalytically active hydride species and corresponding intermediates *in situ.* Notably, our work provides evidence for the formation of an extended network of Rh complexes and identifies stabilizing effects of the xantphos and $[NTf_2]^-$ ligands.

2. Experimental part

2.1. Preparation of SILP catalyst and reactor experiments

Catalyst synthesis involved the calcination of 5.00 g of silica gel with 150 Å pore size specification (315–500 μm particle size) at 600 °C for 8 h. The silica support was weighed into a Schlenk flask and 2.162 g of $[C_4C_1Im][NTf_2]$ was added. The Schlenk flask was then evacuated, flushed multiple times with Ar and placed inside an Ar-inertized glove box (Vacuum Atmospheres Company, model: OMNI-LAB). Inside the glove box, we added 0.0243 g of $[Rh(acac)(CO)_2]$ and 0.219 g of xantphos. Around 15 ml of anhydrous dichloromethane (DCM) was used as a solvent and added to the Schlenk flask inside a fume hood. A Schlenk line was used to ensure O_2-free atmosphere in the flask. Then, an Ar-inertized rotary evaporator was used to thoroughly mix all the components before the solvent was removed at 40 °C and 800 mbar for 1 h. The Schlenk flask was again flushed with Ar and stored inside the glove box This leads to a volumetric pore filling degree $\alpha_{IL} = 0.3$ according to eqn (2).

$$\alpha_{IL} = \frac{V_{IL}}{V_{Pore}} \tag{2}$$

The molar ratio of xantphos to $[Rh(acac)(CO)_2]$ was 4 : 1 and the metal loading was 0.002 $g_{Rh}\ g_{silica}^{-1}$. Detailed information on all reagents can be found in the SI Table S1.

Hydroformylation of ethylene was carried out in the gradient-free gas-recycle Berty reactor. The Berty reactor consists of a round, stainless-steel casing, inside of which is a round catalyst basket (see Fig. 1a). The gas inlet is located right below the catalyst basket and the turbine that continuously stirs the gas mixture is directly above it (see Fig. 1b).[18] Rotation of the turbine at >5000 rounds per minute ensures fully backmixed behaviour. Glass wool was placed in the catalyst basket and 1.00 g of the prepared catalyst was deposited from the top followed by another layer of glass wool (see Fig. 1c). A steel wire mesh was placed below and above the glass wool to keep the catalyst in place. The catalyst basket was then placed inside the reactor and quickly purged with helium. The reactor was then sealed, and a leak test was carried out with helium (12 bar).

The feed gas flow rates and temperature ramp were set using FlexLab software. The product gas stream was analyzed using gas chromatography (GC, Varian 3900) with a flame ionization (FID) detector and a PoraPLOT Q-HAT column (30 m × 0.32 mm). The conversion X and turnover frequency (TOF) were calculated as per the eqn (3)–(5) based on the peak areas obtained from the GC signals and the flowrates. The peak area corresponding to each component in the product stream was identified and divided by the response factor to obtain the conversion.[19] The amount of Rh (n_{cat}), was calculated by dividing the mass of Rh precursor, $[Rh(acac)(CO)_2]$, added to the catalyst by its molar mass (258.03 g mol^{-1}).

$$X = 1 - \frac{c_{Ethene}}{c_{Ethene,0}} = 1 - \frac{\frac{A_{Ethene}}{2}}{\frac{A_{Ethene}}{2} + \frac{A_{Ethane}}{2} + \frac{A_{Propanal}}{3} + \frac{A_{C_6}}{6}} \tag{3}$$

$$\dot{n}_{Ethene,0} = \frac{p\dot{V}}{RT} = \frac{1\ \text{bar}\ 15\ \text{ml}_n\ \text{min}^{-1}}{8.314\ \text{J mol}^{-1}\ \text{K}^{-1}\ 29\,215\ \text{K}} 60\ \text{min h}^{-1} = 0.03705\ \text{mol h}^{-1} \tag{4}$$

$$\text{TOF} = \frac{X\dot{n}_{Ethene,0}}{n_{cat}} \tag{5}$$

2.2. Transmission infrared spectroscopy (TIRS)

TIR spectra were recorded using an ALPHA II compact FT-IR spectrometer (Bruker) in combination with a TIRS module, a KBr beam splitter and DLaTGS detector. We first recorded a

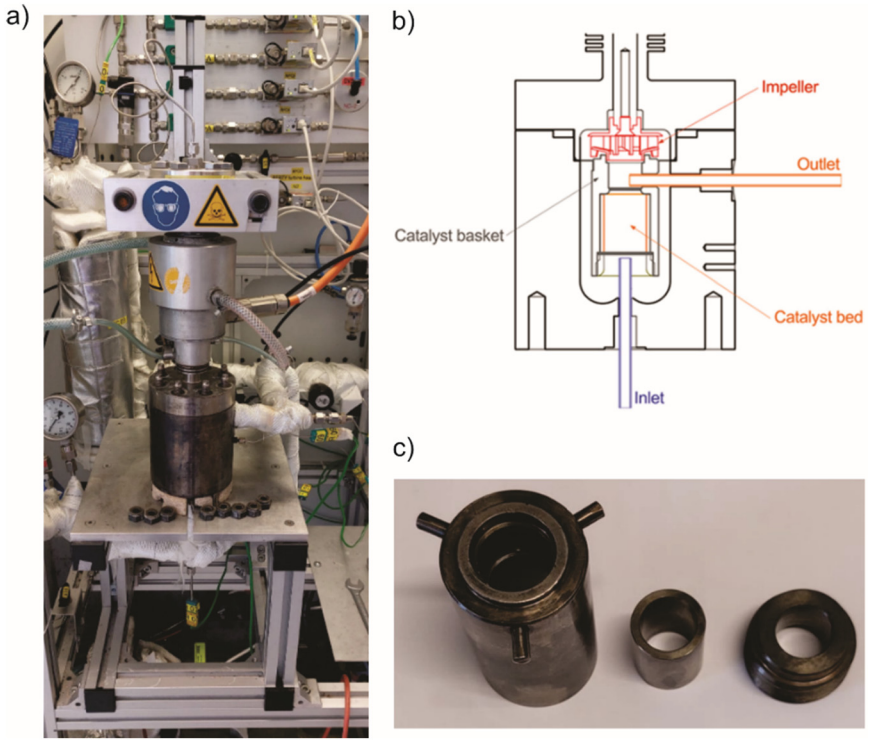

Fig. 1 Berty reactor setup: a) Berty reactor with part of the gas feed system, b) schematic cross section of the Berty reactor,[18] c) catalyst basket with its internal casing.

spectrum of pure DCM in a liquid transmission cell (Pike) as background (256 scans). Subsequently, we analyzed DCM solutions of the pristine SILP components ([Rh(acac)$(CO)_2$], xantphos, [C_4C_1Im][NTf_2]) as well as their mixtures. More detailed information *e.g.* concerning the respective concentrations can be found in the SI Table S2. Sample spectra were recorded with 28 scans per spectrum, resulting in an acquisition time of 57 s per spectrum. For all spectra, we applied a resolution of 2 cm^{-1} and a scanner velocity of 40 kHz.

2.3. Infrared reflection absorption spectroscopy (IRAS)

We performed all temperature-programmed (TP-)IRAS experiment using a Vertex 80v spectrometer (Bruker). The spectrometer is equipped with a KBr beam splitter and a liquid N_2-cooled HgCdTe-detector. IRAS spectra were acquired continuously (resolution = 2 cm^{-1}; acquisition time = 1 min). The IRAS reactor is connected externally to the spectrometer and features all electrical and gas dosing connections required. Please note that the complete beam path remains evacuated during the measurement which results in a high stability of the system. The samples are placed on a Ta sample holder inside of the IRAS reactor. The Ta holder includes a SiC plate on the bottom of the sample holder which is in direct contact with the sample. A glass fibre cable focusses the heating laser (980 nm, 140 W Nd:YAG IR laser diode, JOLD-140-CPXF-2P-W, Jenoptik) through the bottom window (Suprasil 3001, Korth) onto the SiC plate, thus providing efficient heating of the sample. To read the temperature, a type K thermocouple is in direct contact with the sample. Finally, the stainless-steel IRAS reactor is water-cooled to compensate for the indirect heating of the reactor housing.

An elaborate gas system is connected to IRAS reactor, gas dosing is controlled by five mass flow controllers (MFCs, all from Bronkhorst). The combination of different types of MFCs allows to control the gas flow precisely up to 20 mL_N min^{-1}. H_2 (Linde, >99.999%), Ar (Linde, >99.999%), CO (Linde, >99.997%), and ethylene (Linde, minican, >99.5%) were used within this work. Further purification of the CO gas stream was achieved by passing through a consecutive carbonyl trap (Gaskleen II Purifier from Pall Corporation).

Before the IRAS measurements, the IL solutions was all freshly prepared, the detailed components can be found in SI Table S3.

Fig. 2 illustrates the preparation of the SILP wafer in the reactor. Initially, we place a customized SiO_2 beads wafer (see below) into the IRAS chamber in Ar atmosphere (1 bar, 3.57 mL min^{-1}). Next, we applied 20 µL of the respective DCM solution on the center of the wafer using a GC injector (see Fig. 2a). Subsequently, apply the reactant gas mixture at 1 bar (see Fig. 2b) and continuously heat the sample from 30 °C to 200 °C at a rate of 2 K min^{-1} using a fully automatized procedure (see Fig. 2c, for details on the heating ramp and applied gas atmosphere see SI, Fig. S1). After the completion of the heating ramp, the reactor cell was cooled down, shortly evacuated to remove all the gas in the system, and then

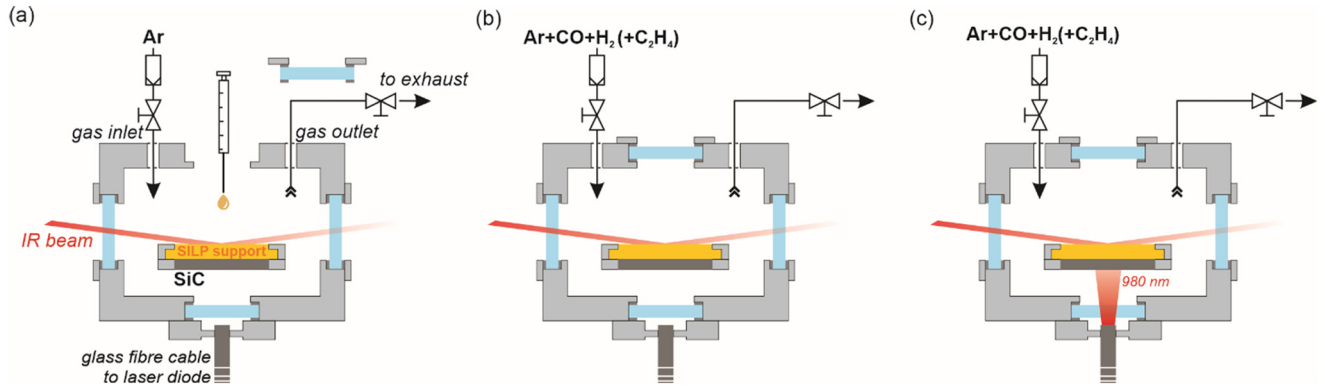

Fig. 2 Preparation of SILP wafer TP-IRAS measurement: a) application of IL solution on SiO_2 bead wafers, b) introduction of reaction atmosphere, c) laser heating of the sample and performance of TP-IRAS procedure.

purged with 1 bar Ar (3.57 mL min^{-1}). We apply a fresh SiO_2 beads wafer for each IRAS experiment.

2.4. Preparation and characterization of SiO_2 beads wafers

Silicon wafers (P/Bor, <100>, SSP, 675 ± 25 µm, CZ, 150 ± 5 mm, 1–100 Ohm cm^{-1}, Active Business Company, Germany) with a native SiO_2 layer of about 2 nm were cleaned with ethanol, dried under N_2 and cut into pieces of 1 × 1 cm in size. The wafers were coated with a 100 nm thick Au layer (HMW Hauner, 99.99%, <3 mm granulate) using a custom-built thermal evaporator (Torr International Inc, THE3-KW). The samples were exposed to an O_2 plasma (Femto, Diener Electronics, 100 W, 10 min, 5 sccm oxygen) and immersed into an aqueous 0.1 wt% solution of LudoxTM (particle size 22 nm, Sigma Aldrich) particles for 5 min. Upon drying *via* evaporation of water, a layer of particles was deposited onto the substrate. The samples were analyzed by contact angle measurement (droplet volume: H_2O 2.5 µL and $[C_4C_1Im][NTf_2]$ 2 µL, Drop Shape Analyzer DSA25E, Krüss Germany) and scanning electron microscopy (SEM, GeminiSEM 500, Zeiss Germany) and stored under ambient conditions. For the sessile drop measurements, ultrapure H_2O and $[C_4C_1Im][NTf_2]$ were applied. Before deposition onto these customized substrates, the IL was dried *in vacuo* for 24 h.

2.5. Density functional theory calculations

Geometry optimizations were performed with Gaussian16 at the BP86-D3 (ref. 20–23) level of theory in combination with the def2-TZVP[24] basis set. All stationary points were fully characterized as minima (only positive eigenvalues). A Gaussian broadening of 10 cm^{-1} and a scaling factor of 1.012 (see ref. 25) was applied to all visualized DFT-computed IR spectra. This leads to an excellent agreement between the experimental and DFT-computed spectra (see Fig. S2). To account for the flexible nature of the species involved, we performed initially a conformational sampling at the GFN2-xTB level of theory with the CREST (2. 12) program system.[26,27] Constraints were used to avoid ligand dissociation and to ensure appropriate sampling of the isomers in the gas phase. Identified minimum energy conformers of each isomer were subsequently optimized at the DFT level of theory. In order to test whether the addition of diffuse functions would influence the prediction of IR spectra, we performed additional calculations with the ma-def2-TZVP basis set on a subset of the anionic species. The addition of diffuse functions did not influence the resulting IR spectra and in order to reduce the calculational overhead, we, therefore, did not include diffuse functions in the calculations of the IR spectra. In order to obtain energy profiles of key steps along the reaction mechanism, the involved structures were reoptimized with the SMD-GIL[28] solvation model for $[C_4C_1Im][NTf_2]$ at the RI-BP86-D3/def2-TZVP level including diffuse functions from the ma-def2-TZVP basis set[29] on the phosphor atoms of xantphos, rhodium and all atoms of the other ligands, hereafter for convenience simply referred to as ma-def2-TZVPP. All transition structures were obtained by means of climbing-image nudged-elastic-band calculations as implemented in Orca.[30] Thermochemical corrections to the electronic energy were computed at the same level of theory utilizing the standard formalism. Domain based local pair natural orbit (DLPNO)-CCSD(T)/ma-def2-TZVPP single point calculations were performed with ORCA utilizing automatically generated auxiliary basis sets and tight PNO settings.[31] The RIJCOSX formalism was applied to speed up the SCF calculations.[32] Computed multi-reference diagnostics for the species involved were found to be in the acceptable range for transition metal complexes (see SI Table S4)[33,34] and are similar in magnitude to previous works on transition metal catalyzed reactions.[14,35,36] Additional single point calculations at the ωB97M-V/ma-def2-TZVPP[37] level of theory were conducted without RI approximations.

3. Results and discussion

3.1. Evaluation of catalysts performance

We studied the hydroformylation of ethylene between 80 and 100 °C in a gradient-free Berty reactor, which provides highly reproducible results for these studies (see SI Fig. S3). We use SILP catalysts consisting of $[Rh(acac)(CO)_2]$ + xantphos/$[C_4C_1Im][NTf_2]/SiO_2$ with 0.2 wt% Rh loading and a Rh : xantphos ratio of 1 : 4 to overcompensate for potential interactions between

xantphos and SiO_2.[38] Furthermore, we apply an IL loading α_{IL} = 30% to ensure complete wetting of the surface of the SiO_2 support with the SILP phase.[39] Fig. 3a shows the conversion and turnover frequency at each temperature. The average conversion of ethylene is 1.6% (80 °C), 4.3% (90 °C), and 12.0% (100 °C) in the examined temperature windows, respectively. This indicates that the catalyst is already slightly active at 80 °C with a more pronounced increase in ethylene conversion above 90 °C. The apparent activation energy calculated from these temperatures was 107 kJ mol^{-1} (see Fig. 3b). The calculated apparent activation energy is of the same magnitude as in studies from Qi *et al.*, who reported an apparent activation energy of 90 kJ mol^{-1} for bimetallic Rh–Co-catalyzed ethylene hydroformylation.[40] These results confirm that this system maintains steady-state conversion of ethylene without any signs of degradation of the molecular Rh complex. Therefore, we apply the same catalyst composition with an identical ratio of [Rh(acac)(CO)$_2$] : xanthpos : [C_4C_1Im][NTf_2] in our TP-IRAS studies.

3.2. Speciation of the Rh complex in the as-prepared IL phase

In order to understand transformations of the Rh complex under reaction conditions, we first need to analyze in detail the molecular interactions between the SILP components: the catalyst precursor [Rh(acac)(CO)$_2$], the stabilizing xanthpos ligand, and [C_4C_1Im][NTf_2]. This includes, in particular, changes in the ligand sphere of the active Rh metal that already arise during preparation of the SILP.

To this aim, we recorded reference spectra for the individual SILP components and their mixtures in TIRS mode. Please note that we reduced the amount of [C_4C_1Im][NTf_2] as compared to the SILP used in the Berty reactor experiment to prevent total absorption of the IL bands in the IR spectra. To investigate the effect of varying the IL content, we examined two mixtures of [Rh(acac)(CO)$_2$] with [C_4C_1Im][NTf_2] in molar ratios of 1 : 10 and 1 : 25. Fig. 4 shows the resulting spectra. In Fig. 4a, we identify characteristic IR bands of the individual components. The IL cation $[C_4C_1Im]^+$ shows a band at 1422 cm^{-1} from $\delta(CH_x)$, while the $[NTf_2]^-$ anion has several, more pronounced bands: 1350 cm^{-1} ($\nu(SO_2)_s$ + $\nu(CF_3)_s$), 1197 cm^{-1} (ν(CS) + $\nu(CF_3)_s$), 1137 cm^{-1} ($\nu(CF_3)_{as}$ + $\nu(SO_2)_s$), and 1059 cm^{-1} ($\nu(SNS)_{as}$ + $\nu(CF_3)_s$ + $\nu(SO_2)_s$).[41,42] For [Rh(acac)(CO)$_2$] (**1**), the TIR spectrum shows two pairs of peaks. The bands at 2083 and 2011 cm^{-1} corresponds to the ν(CO) vibrations from the two CO ligands (highlighted in blue). The second pair at 1568 and 1526 cm^{-1} relates to $\nu(acac_{ring})$ and ν(CCC) vibrations of the acac ligand. The sharp peak around 1403 cm^{-1} is due to the *P*-phenyl vibration in xantphos.[43] Note that the sharp feature at 1270 cm^{-1} results from total absorption of the DCM solvent and has been greyed out in the spectra to facilitate the discussion. The experimental and DFT-computed spectra of xantphos and [Rh(acac)(CO)$_2$] (**1**) are in excellent agreement as shown in Fig. S2.

Next, we evaluate the spectra of the mixtures shown in Fig. 4b. The spectrum of the solution of [C_4C_1Im][NTf_2] + xantphos is a simple combination of the bands of the individual components suggesting that no chemical interactions between both species occur. In all mixtures containing [Rh(acac)(CO)$_2$], however, we see changes in the peak intensities and the appearance of new peaks. This suggests that the chemical state of the Rh precursor changes when the SILP system is prepared. We summarize all newly observed bands, their proposed assignment, and comparison with the respective DFT-derived bands in Table 1.

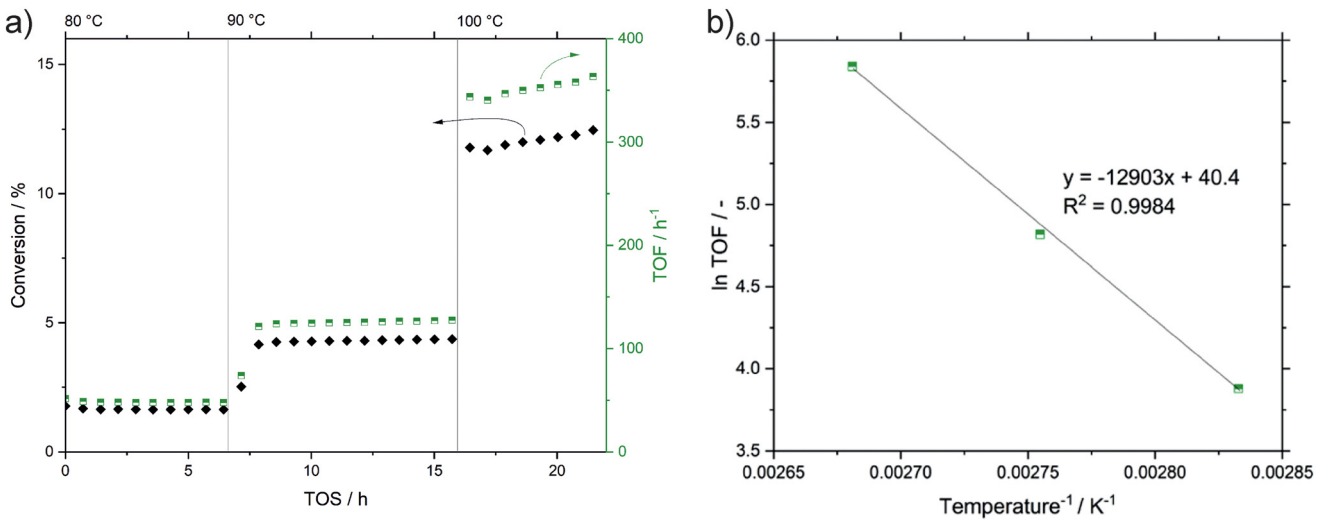

Fig. 3 Hydroformylation of ethylene in a Berty reactor using a SILP catalyst consisting of [Rh(acac)(CO)$_2$] : xantphos in a ratio of 1 : 4 dissolved in [C_4C_1Im][NTf_2] and supported on silica 150, particle size 350–500 μm, IL loading α_{IL} = 30%. a): Ethylene conversion (black diamonds) and turnover frequency (TOF, green squares) at 80, 90, and 100 °C; b): corresponding Arrhenius plot. Reaction conditions: 1.0 g catalyst, 0.2 wt% Rh, *T* = 80–100 °C, *p* = 1.1 MPa, 15 ml_N min^{-1} C_2H_4, 30 ml_N min^{-1} H_2, 30 ml_N min^{-1} CO, average residence time 185 s.

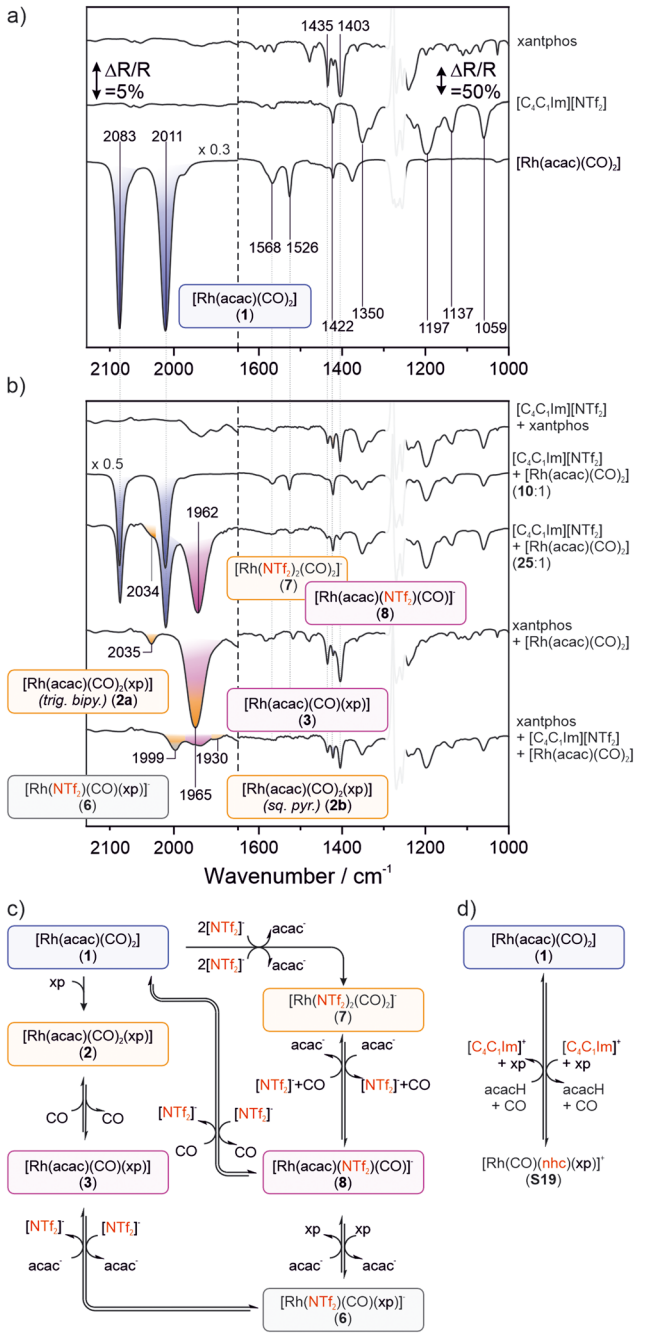

Fig. 4 Speciation in the SILP: TIR spectra for a) $[Rh(acac)(CO)_2]$, $[C_4C_1Im][NTf_2]$ and xantphos (xp) and b) their mixtures measured under ambient conditions in DCM (refer to Table S2 in SI for the preparation of the respective solutions); c) proposed network of ligand exchange reactions. d) Alternative formation of NHC complexes following an oxidative addition of $[C_4C_1Im]^+$.

In the $[C_4C_1Im][NTf_2]$ + $[Rh(acac)(CO)_2]$ solution, the characteristic peaks of the CO (2083/2011 cm^{-1}) and acac (1568/1526 cm^{-1}) ligands are smaller as compared to the spectrum of pure $[Rh(acac)(CO)_2]$. Concerning the ratio of carbonyl band intensities, we observe a slight increase of the band at 2011 cm^{-1}. In addition, a new peak appears at 1962 cm^{-1} at a higher IL content. Based on DFT calculations, we assign this band to the anionic complex $[Rh(acac)(NTf_2)(CO)]^-$ (**8**), which is formed by a ligand exchange between CO and $[NTf_2]^-$. Furthermore, the spectrum shows a shoulder at 2034 cm^{-1} (see Fig. S4 in SI for better visualization) which we attribute to the formation to $[Rh(NTf_2)(CO)_2]^-$ (**7**). The observed band position aligns best with a *trans* isomer (**7c**, Δ = −15 cm^{-1}), while the computed thermochemistry favours the *cis*, κN isomer (**7a**), which is predicted to show an additional weaker band at higher wavenumber that could indeed be hidden by the bands of $[Rh(acac)(CO)_2]$ (**1**). In our previous studies, we observed similar ligand exchange reactions between CO and other IL anions such as Cl^-.[13] However, the current data suggest that $[NTf_2]^-$ is not only able to replace CO, but also the bidentate acac ligand to a lesser extent. This highlights that the IL is not only an "innocent" solvent but actively influences the speciation of the molecular Rh complex. The increase in peak intensity at higher IL : Rh ratio indicates that the amount of the majority species $[Rh(acac)(NTf_2)(CO)]^-$ (**8**) increases when more $[NTf_2]^-$ ligands are available. Furthermore, the presence of charged species in the local environment of the intact $[Rh(acac)(CO)_2]$ (**1**) may induce slight geometric changes to the complex (*e.g.* change in bond angles) that in turn can result in changes of the CO band intensities. We additionally evaluated the possible formation of *n*-heterocyclic carbene (NHC) complexes from the $[C_4C_1Im]^+$ cation as suggested by Nolan,[44,45] however, we find only a poor fit with the experimental data (see Table S8 in SI). Indeed, carbene formation in deuterated $[C_4C_1Im][NTf_2]$ ILs under similar conditions has been investigated in the past by Scholten and Dupont.[46] They observed only transient carbene formation and only in presence of the phosphine. They showed that presence of some amounts of MeOH, serving as a weak base, significantly increases the carbene formation. However, their work highlights that the precursor $[Rh(acac)(CO)_2]$ alone did not form carbenes even in the presence of a weak base. This indicates that *in situ* carbene formation from $[C_4C_1Im]^+$ affords a metal complex with either xantphos or other phosphine-based ligands and might follow an oxidative addition reaction.[47] Our results show that the ligand exchange takes place in a dynamic equilibrium and is enhanced at higher concentrations of $[C_4C_1Im][NTf_2]$, which is particularly true for the real SILP material.

The spectrum of the mixed solution of xantphos and $[Rh(acac)(CO)_2]$ does not show the characteristic CO peaks of $[Rh(acac)(CO)_2]$ (**1**) and the acac bands are largely suppressed. In addition, a new, intense band appears at 1965 cm^{-1}, which is assigned to [Rh(acac)(CO)(xp)] (**3**). Furthermore, this peak, together with the smaller signal at 2035 cm^{-1} indicates a small amount of $[Rh(acac)(CO)_2(xp)]$ (*trig. bipy.*) (**2a**). The corresponding changes in the bands of the acac ligand confirm both assignments (see SI Fig. S6 and Table S6). Note that in both species, xantphos coordinates in monodentate binding mode, similar to other phosphine species.[48] In general, xantphos is regarded as a structurally versatile ligand with report of mono-, bi-, and even tridentate complexes

Table 1 Peak assignment *via* DFT, all wavenumbers in cm^{-1}, for more detailed data on different isomers of species (**7a–b**), (**9a–d**) and (**10a–b**) see SI, Tables S5 and S8

Nr.	Species	ν_{exp}		ν_{DFT}		$\nu_{DFT} - \nu_{exp}$
1	$[Rh(acac)(CO)_2]$	2011		2021 (*vs*)		10
		2083	$\Delta = 72$	2085 (*vs*)	$\Delta = 64$	(−2)
2a	$[Rh(acac)(CO)_2(xp)]$ (*trig. bipy.*)	1965		1984 (*vs*)		19
		2035	$\Delta = 70$	2040 (*vs*)	$\Delta = 56$	5
2b	$[Rh(acac)(CO)_2(xp)]$ (*sq. pyr.*)	1930		1929 (*vs*)		(−1)
		1999	$\Delta = 69$	2000 (*s*)	$\Delta = 71$	1
3	$[Rh(acac)(CO)(xp)]$ (*sq. pyr.*)	1965		1968 (*vs*)		33
4	*Distal*-$[HRh(CO)_2(xp)]$ (*ee*)	<1975		1949 (*w*)		>(−26)
		1990	$\Delta > 15$	1989 (*vs*)	$\Delta = 40$	(−1)
		<2075	$\Delta < 85$	2059 (*m*)	$\Delta = 70$	>(−16)
5	*Distal*-$[HRh(CO)(xp)]$ (*cis*)	1975		1986 (*vs*)		11
6	*Distal*-$[Rh(NTf_2)(CO)(xp)]^-$ (*trans*, *kO*)	1999		2000 (*vs*)		1
7a,c	$[Rh(NTf_2)_2(CO)_2]^-$	2034		2019/2018 (*vs*)		(−15)/(−16)
		~2083	$\Delta = 49$	2089 (*vs*)	$\Delta = 70/64$	~6
8	$[Rh(acac)(NTf_2)(CO)]^-$	1962–65		1978 (*vs*)		16–13
9a–d	$[HRh(NTf_2)(CO)(xp)]^-$	<1975		~1941 (*vs*/*w*)		>~(−34)
		2016	$\Delta > 41$	2015/2028 (*w*)	$\Delta = 74–141$	(−1)/12
		&2075	$\&\Delta > 100$	&2063/2081 (*w*)	$\&\Delta = 122–140$	&(−12)/6
10a	*Distal*-$[Rh(CO)_2(nhc)(xp)]^+$ (*ea*)	1975		1976 (*vs*)		1
		2016	$\Delta = 41$	2018 (*vw*)	$\Delta = 42$	2

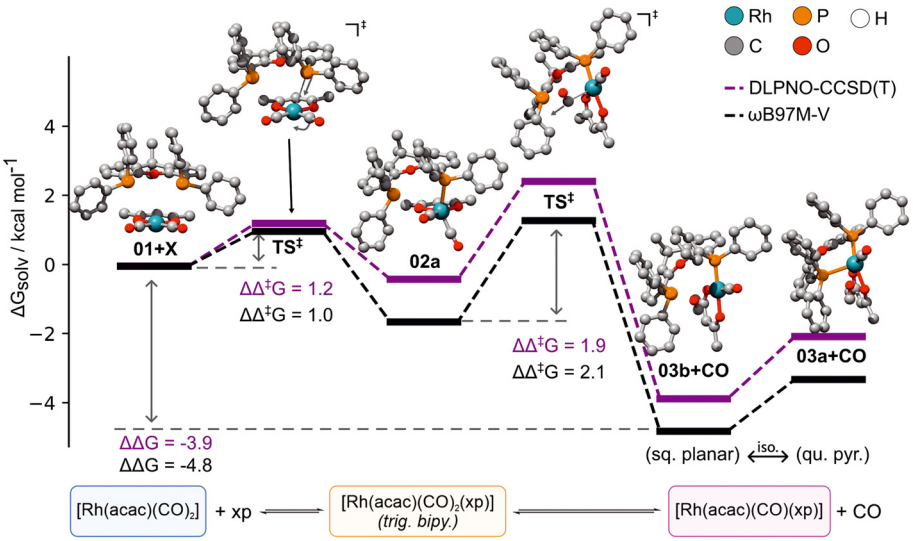

Fig. 5 *Ab initio* reaction profile of the formation of the catalyst precursors in $[C_4C_1Im][NTf_2]$ after mixing $[Rh(acac)(CO)_2]$ and xantphos. Final energies are computed with the ma-def2-TZVPP basis set as described in the method section. Thermal corrections to free energies were computed at the BP86-D3/ma-def2-TZVP + SMD level of theory.

depending on the metal center and counter ligands.[49–53] Our DFT and *ab initio* calculations reveal that the addition of xantphos to $[Rh(acac)(CO)_2]$ is an exothermic process with a very low energy barrier of only +1.0 kcal mol^{-1} (Fig. 5). The following CO elimination is even more exothermic with a similarly low energetic barrier of +2.0 kcal mol^{-1}. According to our calculations, the overall process to form [Rh(acac)(CO)(xp)] (**3**) has a reaction energy of −4.0 to −5.0 kcal mol^{-1}. To the best of our knowledge, the formation of possible intermediates during the formation of [Rh(acac)(CO)(xp)] (**3**) has not been studied before. Surprisingly, we observe $[Rh(acac)(CO)_2(xp)]$ (**2**) as a possible intermediate, which is thermodynamically favoured and might coexist as transient species in the IL solution to some small extent. In the gas phase, the formation of $[Rh(acac)(CO)_2(xp)]$ (**2**) is slightly endergonic, which showcases the stabilising effect of the IL (see Fig. S23 in SI) in this process. Note that the resulting complex [Rh(acac)(CO)(xp)] (**3b**) has a square planar geometry but can be easily converted to the square pyramidal analogue by coordination of xantphos' second leg to give the experimentally observed complex [Rh(acac)(CO)(xp)] (**3a**).

Overall, energetics derived from DFT corroborate our results from the TIRS spectra. Both indicate that [Rh(acac)$(CO)_2$] (**1**) converts immediately upon addition of xantphos

and [Rh(acac)(CO)(xp)] (**3**) becomes the majority species in the solution in line with previous studies on xantphos-based systems.[54–56] The addition of $[NTf_2]^-$ to $[Rh(acac)(CO)_2]$ (**1**) and subsequent elimination of CO to form $[Rh(acac)(NTf_2)(CO)]^-$ (**8**) is, in contrast, estimated to be endothermic with a reaction energy of +21.0 kcal mol^{-1} at the ωB97M-V level of theory (see SI Fig. S5). It is noteworthy that the final energetics obtained at the DLPNO-CCSD(T) and ωB97M-V level of theory are very close to each other. Therefore, we used the ωB97M-V level of theory for all other calculations, as it is known to perform well for transition metal complexes.[57]

The spectrum of the solution containing $[Rh(acac)(CO)_2]$, xantphos, and $[C_4C_1Im][NTf_2]$ shows two comparatively small peaks at 1999 cm^{-1} and 1965 cm^{-1} as well as a weak feature at 1930 cm^{-1}. Since both $[NTf_2]^-$ and xantphos are available for ligand exchange reactions, we compared the DFT-derived bands of the corresponding Rh complexes and found very good agreement with several complexes. We assign the band at 1999 cm^{-1} to $[Rh(NTf_2)(CO)(xp)]^-$ (**6**) and [Rh(acac)$(CO)_2$(xp)] (*sq. pyr.*) (**2b**), the latter also leading to the smaller band at 1930 cm^{-1}. This would mean that the IL stabilizes a different isomer of $[Rh(acac)(CO)_2(xp)]$ (**2**), as it is the case without IL. However, this is not strictly in line with the computed enthalpies at the DFT level which still favour **2a** in solution (see Table S8 in SI). The band at 1965 cm^{-1} is assigned to [Rh(acac)(CO)(xp)] (**3**), however, it is likely that $[Rh(acac)(NTf_2)(CO)]^-$ (**8**) is also present, as observed in the mixture of $[Rh(acac)(CO)_2]$ and $[C_4C_1Im][NTf_2]$, which was described previously. Due to dynamic nature of ligand exchange reactions and the similar spectral characteristics of the resulting complexes, it is strongly expected that several species coexist in solution. Again, considering previous works regarding the formation of NHC complexes in imidazolium based ILs,[46] we also investigated the possible formation of carbenes derived from respective complexes involving xantphos as a ligand. Particularly the complexes of type *distal*-$[Rh(CO)(nhc)(xp)]^+$ (*cis*/*trans*) (**S19**) showed respective peaks in the range 2000–2009 cm^{-1}, which could be in agreement with the experimentally observed band at 1999 cm^{-1}. Assuming a simple oxidative addition reaction and formation of acacH (Fig. 4d), we were also able to compute the reaction energy of the formation of the NHC complexes, which is exothermic and in the range of −19 to −24 kcal mol^{-1}. Since NHC formation usually affords higher temperatures[47] or hydroformylation reaction conditions,[46] it is unlikely but cannot be fully excluded.

Our data shows that there are molecular interactions between the components of the SILP catalyst that induce changes in the speciation of the Rh complex. In addition to the expected replacement of the acac ligand by xantphos, our systematic experiments and DFT calculations show that xantphos can also replace the more strongly bound CO ligand.[58,59] This ability extends to some extent to the IL anion $[NTf_2]^-$. As a result, DCM solutions of the SILP components contain several Rh complexes that can dynamically interconvert *via* ligand exchange reactions. The species identified in the DCM solution including $[Rh(NTf_2)(CO)(xp)]^-$ (**6**), $[Rh(acac)(CO)_2(xp)]$ (**2**), [Rh(acac)(CO)(xp)] (**3**), and $[Rh(acac)(NTf_2)(CO)]^-$ (**8**) presumably also form during the preparation of the SILP and are regarded as the new precursor complexes for the catalytic process. These results are supported by systematic experiments and extensive DFT calculations, including calculations for relevant isomers. Given the chemical similarity and possible interconversion of species in SILP solutions, an unambiguous assignment of all bands remains challenging, and a minor unidentified species cannot be ruled out. The present analysis is our best evidence-based interpretation to date, without a claim to completeness.

To further investigate changes caused by reactants and thermal treatment, we apply similar DCM solutions to prepare SILP wafers and examine them in TP-IRAS experiments.

3.3. SiO_2 beads wafers for IRAS experiments

A challenge in designing suitable SILP systems for IRAS experiments is the limited wettability of the IL on the native gold surface, which prevents the formation of a stable IL thin film on the substrate and thus prevents measurements over sufficient amounts of time. To enhance the wettability, we develop custom wafers to ensure good wetting in the IRAS experiments. These wafers consist of four layers as shown in Fig. 6a. A Si wafer serves as the substrate. A thin Ti layer (2 nm) acts as a binder and ensures adhesion between the Si and Au layers. A sufficiently thick, reflective Au coating (100 nm) enables IR measurements in reflection–absorption mode. SiO_2 beads deposited onto the wafer *via* immersion in a solution of Ludox nanoparticles (diameter ~22 nm) further adds roughness to enhance wettability *via* Wenzel wetting[60] and hold the IL phase in place through capillary forces.[61] We subsequently use these modified substrates or the IRAS experiments to provide stable measurement conditions.

Fig. 6b shows a scanning electron microscopy (SEM) image of the surface of Au/Ti-coated wafers (Ti/Au/Si) while Fig. 6c presents the SiO_2 bead-functionalized wafers (SiO_2(22 nm)/Au/Ti/Si) used in the IRAS experiment. These SEM images indicate that a single layer of close-packed SiO_2 beads covers the Au film on the wafer. Importantly, the structure of the SiO_2 beads wafers remains intact after application of the SILP phase and performance of the TP-IRAS measurements with only few perturbations in the packing (see Fig. 6d).

To compare the wetting properties of the Au-coated wafers and SiO_2 bead-functionalized wafers, we performed contact angle measurements with $[C_4C_1Im][NTf_2]$, the results are shown in Fig. 6e and f, respectively. We measured wetting angles of 31.7° ± 0.5° for $[C_4C_1Im][NTf_2]$ for the Au/Ti/Si wafers and 10.2° ± 0.6° on SiO_2-beads/Au/Ti/Si wafers. Further contact angle measurements, including those of ultrapure H_2O and 12 nm SiO_2 beads, can be found in the SI Table S7. These results demonstrate that the presence of surface roughness, implemented through a layer of SiO_2 beads to the

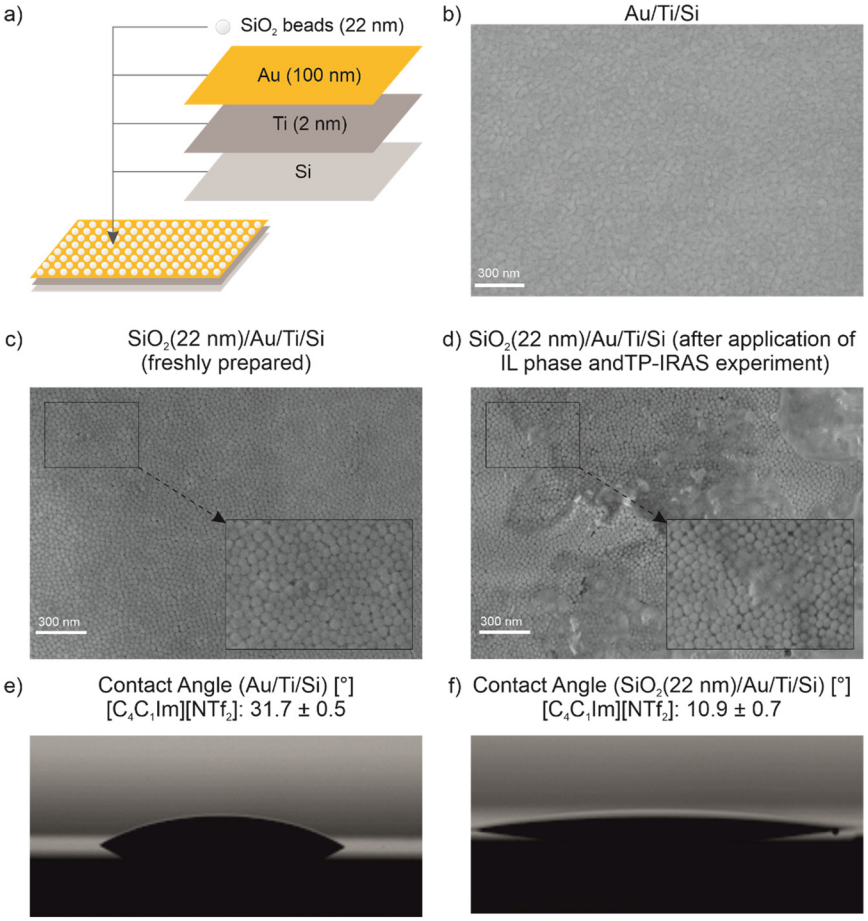

Fig. 6 Characterization of SiO_2 beads wafers: a) scheme and SEM pictures (scale bar = 300 nm) of b) Si wafers coated with a Ti and Au layer (Au/Ti/Si), c) with an additional layer SiO_2 beads (LudoxTM, SiO_2(22 nm)/Au/Ti/Si) wafers before and d) after application of the IL phase and TP-IRAS experiment; contact angle measurements on e) Au/Ti/Si and f) freshly-prepared SiO_2(22 nm)/Au/Ti/Si.

reflective Au/Ti/Si wafers significantly improves the wetting of the SILP phase. The capillary forces between the beads contribute to stabilization of the liquid phase during the TP-IRAS procedure, making the SiO_2 wafers an ideal substrate for IRAS studies.

3.4. Speciation of the Rh complex under reaction conditions

To investigate the speciation of the Rh complex under reaction conditions, we performed *in situ* IRAS on SiO_2-beads/Au/Ti/Si-supported solutions of [Rh(acac)(CO)$_2$], xantphos, and [C_4C_1Im][NTf_2] with varying compositions. We refer to these model systems as SILP wafers in the following. In particular, we investigated SILP wafers of increasing complexity with i) [C_4C_1Im][NTf_2], ii) [Rh(acac)(CO)$_2$] + [C_4C_1Im][NTf_2], and iii) xantphos + [Rh(acac)(CO)$_2$] + [C_4C_1Im][NTf_2]. We exposed these to a reactive gas atmosphere (CO/H2) and gradually heated the system to 200 °C.

In case of the [C_4C_1Im][NTf_2] SILP wafer (see SI Fig. S7), we observe wavy structures >2100 cm^{-1}, which are due to imperfect subtraction of the CO gas phase bands. In addition, fluctuating bands appear at 1930, 1879, 1847, 1801 cm^{-1} when the IL is heated. These bands also appear in the reference spectra of [C_4C_1Im][NTf_2] recorded in attenuated total reflection (ATR) and TIRS mode (see SI, Fig. S8). We attribute the temperature-induced fluctuations to minor changes in the morphology of the [C_4C_1Im][NTf_2] films. Therefore, we expect similar fluctuations in the subsequent experiments with the SILP wafers. For this reason, we will not take the corresponding bands into account for the assignment of Rh complexes.

Fig. 7 shows the temperature-resolved spectra acquired between room temperature (RT) to 200 °C and after cooling back to RT. In each subfigure, the topmost spectrum is the reference spectrum of the unmodified SiO_2 beads wafer, measured at the start of the experiment at RT in 1 bar Ar. The second spectrum was measured after application of the liquid phase. As with the TIRS results, we focus on the CO region of the spectra and identify Rh complexes *via* their CO vibrations. The corresponding IR peaks are highlighted in different colors for easier differentiation.

Fig. 7a displays selected spectra acquired upon heating [C_4C_1Im][NTf_2] + [Rh(acac)(CO)$_2$] on a SiO_2 beads wafer in H_2/CO atmosphere. After adding the IL solution (second

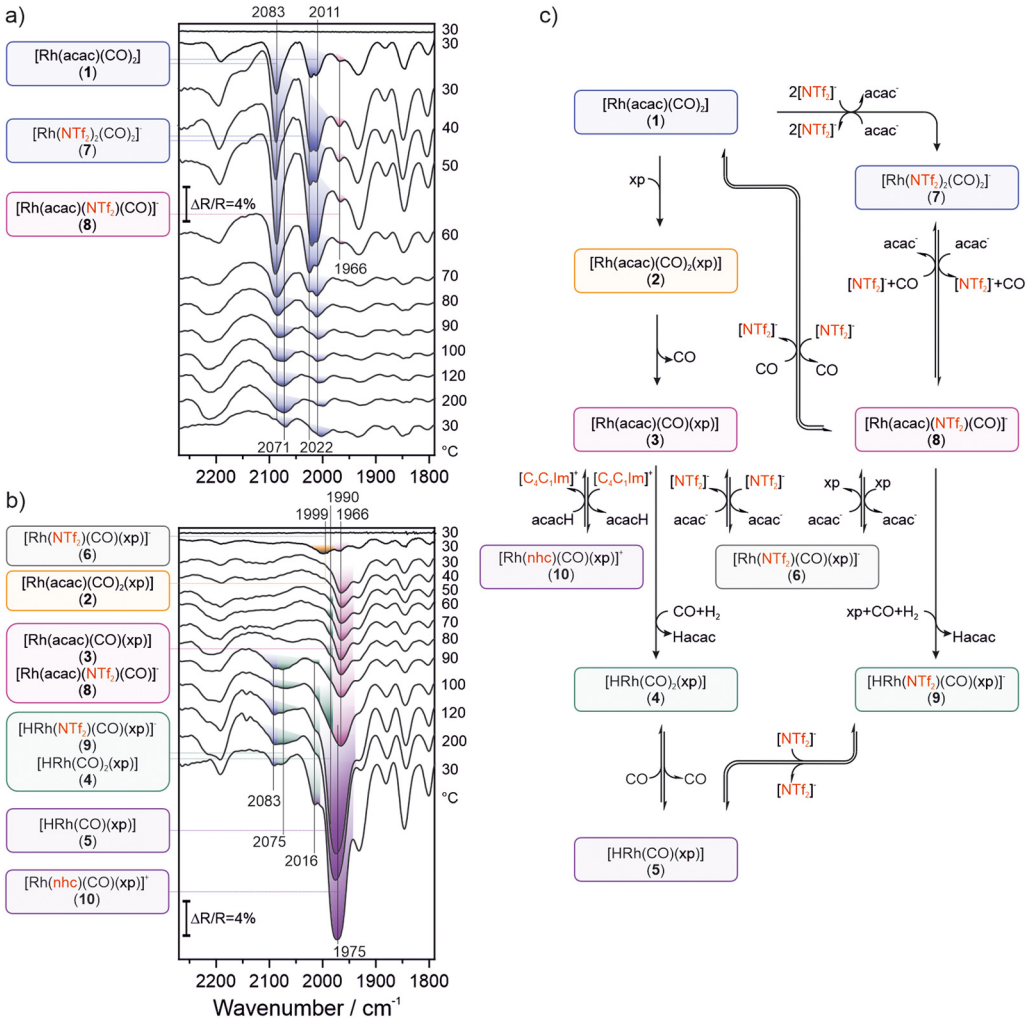

Fig. 7 *In situ* IR spectra of model SILP system under different atmospheres and temperatures: system with: a) $[Rh(acac)(CO)_2]$ + $[C_4C_1Im][NTf_2]$ exposed to CO/H_2; b) xantphos + $[Rh(acac)(CO)_2]$ + $[C_4C_1Im][NTf_2]$ exposed to CO/H_2; post-analysis included subtraction of the CO gas phase according to;[62] c) proposed network of ligand exchange reactions. Reaction conditions: T = 30–200 °C, p = 1 bar, 2.6 ml_N min^{-1} H_2, 0.9 ml_N min^{1} CO, 2.5 ml_N min^{1} Ar.

spectrum from top), we observe a double band at 2083 and 2011 cm^{-1} as well as weaker features at 2071 cm^{-1}, 2022 cm^{-1}, and 1966 cm^{-1}. According to the reference spectra measured in TIRS mode (see Fig. 4), we assign the peaks at 2083 and 2011 cm^{-1} to the intact $[Rh(acac)(CO)_2]$ (**1**) precursor. Ligand exchange with $[NTf_2]^-$ leads to the formation of $[Rh(acac)(NTf_2)(CO)]^-$ (**8**), which results in the smaller band at 1966 cm^{-1}. We attribute the additional pair of bands at 2071 and 2022 cm^{-1} to a Rh complex with two $[NTf_2]^-$ ligands $[Rh(NTf_2)_2(CO)_2]^-$ (**7**), for detailed analysis of different isomers see SI Table S8. This species was not observed in the TIRS measurements, presumably due to the lower IL content. A comparison of the relative peak intensities shows that intact $[Rh(acac)(CO)_2]$ (**1**) remains the majority species in the system at RT. Upon heating the SILP wafer, the intensity of all peaks gradually decreases. This also holds for the IL-related bands at 1930, 1879, 1847, and 1801 cm^{-1}, which suggests that the changes in peak intensity are due to morphological changes of the IL film. We also considered the DFT-derived bands for hydride species (see SI Table S8, species **S5–S9**) that could potentially form and are the catalytically active species in the hydroformylation cycle. Since a few of the predicted bands show reasonable agreement with the experimentally observed bands, their presence in small quantities cannot be completely ruled out. Nevertheless, the overall poor agreement and the fact that these bands would only lie below the signals of the already identified species suggest that the contribution of hydrides to the observed spectrum is negligible.

In summary, we therefore conclude that the Rh precursors $[Rh(acac)(CO)_2]$ (**1**), $[Rh(NTf_2)_2(CO)_2]^-$ (**7**) and $[Rh(acac)(NTf_2)(CO)]^-$ (**8**) do not undergo further conversion in the presence of H_2 and CO, or during heating. Please note that, in accordance with the reactor studies, we do not observe any indication of degradation of the molecular Rh complex into nanoparticles in the DRIFT spectra – this would be apparent from an CO adsorbate band at ~2044 cm^{-1}.[12]

Fig. 7b shows selected spectra recorded during heating of xantphos, $[C_4C_1Im][NTf_2]$ and $[Rh(acac)(CO)_2]$ on a SiO_2 beads wafer in H_2/CO atmosphere. This SILP wafer contains all components of the corresponding real SILP catalyst. After addition the solution dropwise to the wafer, the IR spectrum (second from top) shows two peaks at 1999 and 1966 cm^{-1}. Note that the bands ≤1930 cm^{-1} are not evaluated due to fluctuating signals from the IL. The results agree perfectly with the TIRS results, and in accordance with previous discussion, we assign the observed bands to $[Rh(acac)(CO)_2(xp)]$ (*sq. pyr.*) (**2b**), $[Rh(acac)(NTf_2)(CO)]^-$ (**8**), and $[Rh(NTf_2)(CO)(xp)]^-$ (**6**). Based on the peak intensities, $[Rh(NTf_2)(CO)(xp)]^-$ (**6**) and $[Rh(acac)(CO)_2(xp)]$ (**2**) are the majority species in the system at this stage of the experiment.

With the introduction of the CO/H_2 atmosphere, the peak at 1999 cm^{-1} disappears and the band at 1966 cm^{-1} increases in intensity. At the same time, we observe a shoulder at 1990 cm^{-1}. As the temperature rises, an additional band gradually appears at 1975 cm^{-1}. Above 100 °C, this band strongly increases in intensity at the expense of the peak at 1966 cm^{-1}. In addition, peaks at 2083 cm^{-1} and 2075 cm^{-1} as well as a shoulder at 2016 cm^{-1} appear in the spectra around 90 °C. The decrease in the peak at 1999 cm^{-1} indicates the loss of $[Rh(acac)(CO)_2(xp)]$ (**2**) and $[Rh(NTf_2)(CO)(xp)]^-$ (**6**) in CO/H_2 atmosphere. The gain in intensity of the band at 1966 cm^{-1} in CO/H_2 atmosphere indicates a relative increase of $[Rh(acac)(CO)(xp)]$ (**3**) and $[Rh(acac)(NTf_2)(CO)]^-$ (**8**) in the SILP. These changes point to small variations in speciation upon introduction of the gas phase. We attribute the more severe changes observed upon heating to the formation of hydride species. According to our DFT calculations, the *ee* and *ea* isomer of $[HRh(NTf_2)(CO)(xp)]^-$ (**9**) correspond to the bands at 2075 cm^{-1} and 2016 cm^{-1}, respectively. Both add intensity to the low wavenumber side of the intense band at 1975 cm^{-1}. Moreover, $[HRh(CO)_2(xp)]$ (**4**) is likely to contribute to the bands at 1966 cm^{-1} (at the high wavenumber side) and 2075 cm^{-1} and is responsible for the more pronounced shoulder at 1990 cm^{-1}. The band at 1975 cm^{-1} indicates the formation of $[HRh(CO)(xp)]$ (**5**) through the loss of CO from $[HRh(CO)_2(xp)]$ (**4**). However, the reaction conditions and high temperatures during the IRAS experiments might again be beneficial for the formation of several NHC-based complexes presumably *via* oxidative addition of $[C_4C_1Im]^+$ to a Rh complex in presence of acac and xantphos.[46] Among the computed NHC complexes, $[Rh(CO)_2(nhc)(xp)]^+$ (**10**, in particular the distal, *ea* isomer) exhibits a very strong band at 1976 cm^{-1} which also matches the intense feature at 1975 cm^{-1} observed at elevated temperatures (>100 °C) and persisting after cooling. The second DFT-computed band at 2018 cm^{-1} is also in agreement with the experimental data (band at 2016 cm^{-1}). Assuming an oxidative addition reaction of $[C_4C_1Im]^+$, the enthalpy of this processes also favours NHC formation by −44 to −47 kcal mol^{-1}. Formation of respective NHC-based hydride species was also investigated by DFT. It leads only to poor agreement with the experimentally obtained spectra but cannot be excluded. In particular *distal*-$[HRh(CO)(nhc)(xp)]$ (**S20**) would give rise to bands at 1927–1934 cm^{-1} and weaker bands in the range 1977–1981 cm^{-1}. While the latter bands are in agreement with the experimentally observed band around 1975 cm^{-1}, the experimental data does not allow a clear interpretation of the band around 1930 cm^{-1}. However, it was also noted before that the NHC complexes do neither inhibit the hydroformylation of alkenes nor change the selectivity, which indicates that they are either transient species and/or allow for fast ligand exchanges as soon as the alkene is present under reaction conditions.[46]

Fig. 7c shows a mechanistic overview of the conversion between the identified Rh complexes. The left column illustrates the generally accepted mechanism[5,63] in which the precursor $[Rh(acac)(CO)_2]$ (**1**) binds xantphos *via* ligand exchange and forms $[HRh(CO)_2(xp)]$ (**4**). This complex then loses CO to form $[HRh(CO)(xp)]$ (**5**), the catalytically active species for alkene binding and conversion. Furthermore, we were able to detect the intermediates $[Rh(acac)(CO)_2(xp)]$ (**2**) and $[Rh(acac)(CO)(xp)]$ (**3**) for the first time in this work. Our results also indicate that Rh complexes with $[NTf_2]^-$ ligands are present in considerable amount in the SILP as well. The right column extends the scheme with these species. These include $[Rh(NTf_2)_2(CO)_2]^-$ (**7**) and $[Rh(acac)(NTf_2)(CO)]^-$ (**8**) which immediately form from the $[Rh(acac)(CO)_2]$ precursor and ultimately lead to $[HRh(NTf_2)(CO)(xp)]^-$ (**9**). Note that loss of $[NTf_2]^-$ from $[HRh(NTf_2)(CO)(xp)]^-$ (**9**) also generates the catalytically active species $[HRh(CO)(xp)]$ (**5**). These results lead to two important observations: First, all observed hydride complexes $[HRh(xp)CO]$ (**5**), $[HRh(xp)(CO)_2]$ (**4**), and $[HRh(NTf_2)(CO)(xp)]^-$ (**9**) contain a xantphos ligand. This underscores the role of xantphos ligand not only in stabilizing the molecular Rh complex against degradation, but also as an important factor in the formation of the catalytically active hydride species that which accumulate in the SILP at >100 °C in the absence of the ethylene reactant.

Second, both $[HRh(NTf_2)(CO)(xp)]^-$ (**9**) and $[HRh(CO)_2(xp)]$ (**4**) contain at least one CO ligand, which means that a catalytically active hydride species can be formed from both complexes. While it is well established at this point that $[NTf_2]^-$ can coordinate to Rh to form various complexes, its influence on the energetics of the catalytic hydroformylation mechanism remains unclear. To improve our understanding of the energetics of CO and $[NTf_2]^-$ exchanges within the key intermediates observed in the *in situ* IR spectra, we performed additional DFT calculations. They consider both unbound and bound CO and $[NTf_2]^-$ ligands in the first coordination and solvation shells. In order to obtain reliable starting structures, we screened van der Waals complexes of uncoordinated ligands and different isomers of the $[HRh(CO)_2(xp)]$ (**4**), $[HRh(CO)(xp)]$ (**5**), and $[HRh(NTf_2)(CO)(xp)]^-$ (**9**) with CREST. The most stable complexes where further optimized at the SMD-BP86-D3/ma-def2-TZVP level and final energies obtained with ωB97M-V/ma-def2-TZVPP single point calculations. The results are summarized in

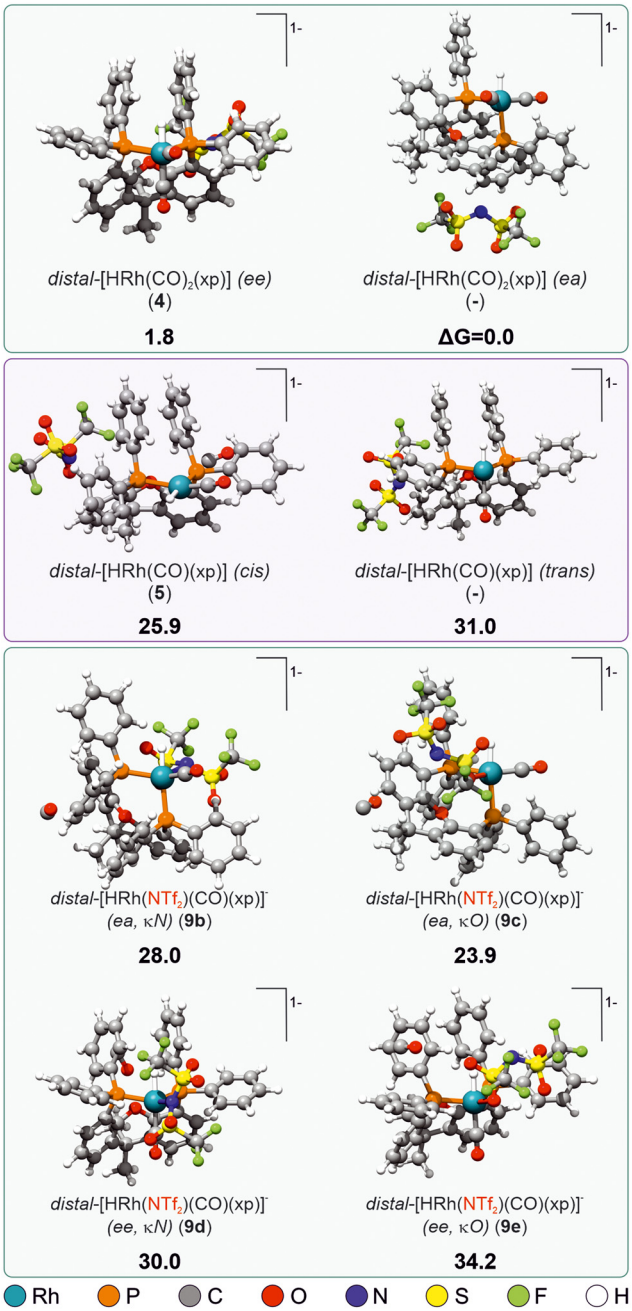

Fig. 8 Calculated relative Gibbs free energies of key hydride species at the SMD-ωB97M-V/ma-def2-TZVPP//SMD-BP86-D3/ma-def2-TZVP level of theory. All species contain equal sets of ligands in either the first solvation or coordination spheres. Energies in kcal mol^{-1} relative to *distal*-[HRh(CO)$_2$(xp)] (*ea*) (**4**).

Fig. 8. The dissociation of CO from species [HRh(CO)$_2$(xp)] (**4**), is endothermic (+25.9 kcal mol^{-1}), with dissociation from the *ea* isomer being energetically more favourable than from the *ee* isomer. This is in line with previous experimental and computational results on the dissociation process.[64] The addition of $[NTf_2]^-$ to the catalytically active hydride [HRh(CO)(xp)] (**5**) *via* the central nitrogen atom seems to be sterically hindered and the resulting complexes are 3–5 kcal mol^{-1} higher in energy than *distal*-[HRh(CO)(xp)](*cis*) (**5a**). However, coordination *via* the oxygen atom has a slight stabilizing effect of 2.0 kcal mol^{-1} for the respective isomer $[HRh(NTf_2)(CO)(xp)]^-$ (**9c**). Contrarily, addition of (NTf_2) to *distal*-[HRh(CO)(xp)](*trans*) (**5c**) favours coordination *via* the nitrogen atom and stabilizes the complex by 1.0 kcal mol^{-1}. Thus, the addition of $[NTf_2]^-$ might contribute to stabilization of the hydride species in the SILP, especially in excess of IL and at higher temperatures. The ability of the $[NTf_2]^-$ anion to participate in the formation of the complex even opens up additional mechanistic pathways for the hydroformylation of small alkenes. However, we cannot categorically rule out the possibility that NHC complexes such as (**10**) are formed under the given reaction conditions and that these complexes largely remain present after cooling.

4. Conclusions

In this study, we investigated the molecular interactions within SILP catalysts for the hydroformylation of ethylene using *in situ* IR spectroscopy and *ab initio* calculations. Our most important findings are summarized below.

The combination of a [Rh(acac)(CO)$_2$] precursor, a four-fold excess of xantphos, [C_4C_1Im][NTf_2], and SiO_2 yields a SILP catalyst that shows stable performance in ethylene hydroformylation and achieves conversion rates of up to 12% at 100 °C.

During the preparation of the SILP material, molecular interactions in the IL phase cause changes in the speciation of the Rh complex. Our investigations reveal an extended network of Rh complexes, including some that have not been reported previously. In particular, xantphos and the $[NTf_2]^-$ anion of the IL act as a ligand and partially replace the CO and acac ligand from the [Rh(acac)(CO)$_2$] precursor. This results in the formation of *e.g.* $[Rh(NTf_2)(CO)(xp)]^-$, [Rh(acac)(CO)(xp)], [Rh(acac)(CO)$_2$(xp)], and $[Rh(acac)(NTf_2)(CO)]^-$. The presence of xantphos in all identified Rh highlights its stabilizing role. The formation of [Rh(acac)(CO)(xp)] with xantphos bound in monodentate fashion is in analogy to other phosphine ligands and was identified as an exothermic process with negligible activation barriers.

We further analyzed changes in the speciation *via in situ* IRAS spectroscopy in reactive atmosphere using specially developed SILP wafers with improved wettability for the IL phase.

In H_2/CO atmosphere, the speciation in the SILP phase presumably further changes towards the formation of hydrides. In particular, we observe the formation of Rh-hydrides with either xantphos and/or $[NTf_2]^-$ ligands *i.e.* [HRh(CO)(xp)], [HRh(CO)$_2$(xp)], and $[HRh(NTf_2)(CO)(xp)]^-$. Formation of $[NTf_2]^-$-containing Rh hydrides can have a stabilizing effect, which may open up new routes for the catalytic hydroformylation cycle. However at elevated temperatures we cannot exclude the formation of NHC-based species from $[C_4C_1Im]^+$ such as [Rh(nhc)(CO)(xp)] which might also persist after cooling to room temperature.

Conflicts of interest

There are no conflicts to declare.

Data availability

The data that support the findings of this study are openly available in Zenodo at https://doi.org/10.5281/zenodo.16759518.

Supplementary information (SI) is available. See DOI: https://doi.org/10.1039/d5cy01282a.

Acknowledgements

This work was funded by the Deutsche Forschungsgemeinschaft (DFG, German Research Foundation) – Project-ID 431791331 – SFB 1452 (CLINT Catalysis at Liquid Interfaces) and Project-ID 530732852. During the preparation of this work the authors used DeepL to improve the language. After using this tool/service, the authors reviewed and edited the content as needed and take full responsibility for the content of the publication.

References

1 C. P. Mehnert, R. A. Cook, N. C. Dispenziere and M. Afeworki, *J. Am. Chem. Soc.*, 2002, **124**, 12932–12933.
2 A. Riisager, P. Wasserscheid, R. Van Hal and R. Fehrmann, *J. Catal.*, 2003, **219**, 452–455.
3 A. Riisager, R. Fehrmann, M. Haumann and P. Wasserscheid, *Eur. J. Inorg. Chem.*, 2006, **2006**, 695–706.
4 M. Haumann and P. Wasserscheid, in *Catalysis in Ionic Liquids: From Catalyst Synthesis to Application*, The Royal Society of Chemistry, 2014, pp. 410–432.
5 J. M. Marinkovic, A. Riisager, R. Franke, P. Wasserscheid and M. Haumann, *Ind. Eng. Chem. Res.*, 2019, **58**, 2409–2420.
6 Z. He, Z. Hou, Y. Zhang, T. Wang, Y. Dilixiati and W. Eli, *Catal. Today*, 2015, **247**, 147–154.
7 I. Tóth, G. Ipin and B. E. Hanson, *J. Mol. Catal. A: Chem.*, 1997, **116**, 217–229.
8 S. I. Fujita, Y. Sano, B. M. Bhanage and M. Arai, *J. Catal.*, 2004, **225**, 95–104.
9 X. Zhang, Y. Du, H. Jiang, Y. Liu and R. Chen, *Catal. Lett.*, 2019, **149**, 3087–3096.
10 A. J. Greer, J. Jacquemin and C. Hardacre, *Industrial Applications of Ionic Liquids*, 2020, vol. 25.
11 T. Welton, *Chem. Rev.*, 1999, **99**, 2071–2084.
12 E. Kratzer, S. Schötz, S. Maisel, D. Blaumeiser, S. Khan Antara, L. Ewald, D. Dotzel, M. Haumann, A. Görling, W. Korth, A. Jess and T. Retzer, *Catal. Sci. Technol.*, 2023, **13**, 2053–2069.
13 T. Bauer, R. Stepic, P. Wolf, F. Kollhoff, W. Karawacka, C. R. Wick, M. Haumann, P. Wasserscheid, D. M. Smith, A.-S. S. Smith and J. Libuda, *Catal. Sci. Technol.*, 2018, **8**, 344–357.
14 P. Wolf, C. R. R. Wick, J. Mehler, D. Blaumeiser, S. Schötz, T. Bauer, J. Libuda, D. Smith, A.-S. Smith and M. Haumann, *ACS Catal.*, 2022, **12**, 5661–5672.
15 R. G. Greenler, *J. Chem. Phys.*, 1966, **44**, 310–315.
16 H. Pearce and N. Sheppard, *Surf. Sci.*, 1976, **59**, 205–217.
17 S. Schernich, D. Kostyshyn, V. Wagner, N. Taccardi, M. Laurin, P. Wasserscheid and J. Libuda, *J. Phys. Chem. C*, 2014, **118**, 3188–3193.
18 M. Cui, S. R. Kulkarni, S. Wagner, C. Berger-Karin, A. Nagy and P. Castaño, *ACS Eng. Au*, 2022, **2**, 103–117.
19 J. T. Scanlon and D. E. Willis, *J. Chromatogr. Sci.*, 1985, **23**, 333–340.
20 A. D. Becke, *Phys. Rev. A: At., Mol., Opt. Phys.*, 1988, **38**, 3098–3100.
21 J. P. Perdew, *Phys. Rev. B: Condens. Matter Mater. Phys.*, 1986, **33**, 8822–8824.
22 S. Grimme, S. Ehrlich and L. Goerigk, *J. Comput. Chem.*, 2011, **32**, 1456–1465.
23 F. Neese, *J. Comput. Chem.*, 2003, **24**, 1740–1747.
24 F. Weigend and R. Ahlrichs, *Phys. Chem. Chem. Phys.*, 2005, **7**, 3297–3305.
25 M. K. Assefa, J. L. Devera, A. D. Brathwaite, J. D. Mosley and M. A. Duncan, *Chem. Phys. Lett.*, 2015, **640**, 175–179.
26 S. Grimme, *J. Chem. Theory Comput.*, 2019, **15**, 2847–2862.
27 P. Pracht, F. Bohle and S. Grimme, *Phys. Chem. Chem. Phys.*, 2020, **22**, 7169–7192.
28 V. S. Bernales, A. V. Marenich, R. Contreras, C. J. Cramer and D. G. Truhlar, *J. Phys. Chem. B*, 2012, **116**, 9122–9129.
29 J. Zheng, X. Xu and D. G. Truhlar, *Theor. Chem. Acc.*, 2011, **128**, 295–305.
30 V. Ásgeirsson, B. O. Birgisson, R. Bjornsson, U. Becker, F. Neese, C. Riplinger and H. Jónsson, *J. Chem. Theory Comput.*, 2021, **17**, 4929–4945.
31 G. L. Stoychev, A. A. Auer and F. Neese, *J. Chem. Theory Comput.*, 2017, **13**, 554–562.
32 F. Neese, F. Wennmohs, A. Hansen and U. Becker, *Chem. Phys.*, 2009, **356**, 98–109.
33 S. Grimme and A. Hansen, *Angew. Chem., Int. Ed.*, 2015, **54**, 12308–12313.
34 J. Wang, S. Manivasagam and A. K. Wilson, *J. Chem. Theory Comput.*, 2015, **11**, 5865–5872.
35 R. Stepić, C. R. Wick, V. Strobel, D. Berger, N. Vučemilović-Alagić, M. Haumann, P. Wasserscheid, A. S. Smith, D. M. Smith, N. Vučemilović-Alagić, M. Haumann, P. Wasserscheid, A. S. Smith and D. M. Smith, *Angew. Chem., Int. Ed.*, 2019, **58**, 741–745.
36 C. R. Wick and D. M. Smith, *J. Phys. Chem. A*, 2018, **122**, 1747–1755.
37 N. Mardirossian and M. Head-Gordon, *J. Chem. Phys.*, 2016, **144**(21), 214110.
38 S. Shylesh, D. Hanna, S. Werner and A. T. Bell, *ACS Catal.*, 2012, **2**, 487–493.
39 M. Frosch, C. L. Tavera Mendez, A. B. Koch, M. Schörner, M. Haumann, M. Hartmann and D. Wisser, *J. Phys. Chem. C*, 2023, **127**, 9196–9204.
40 L. Qi, S. Das, Y. Zhang, D. Nozik, B. C. Gates and A. T. Bell, *J. Am. Chem. Soc.*, 2023, **145**, 2911–2929.

41 C. Schuschke, L. Fromm, J. Träg, C. Stumm, C. Hohner, R. Eschenbacher, S. Grau, D. Zahn, A. Görling, T. Bauer and J. Libuda, *J. Phys. Chem. C*, 2021, **125**, 13264–13272.
42 C. Schuschke, C. Hohner, C. Stumm, M. Kettner, L. Fromm, A. Görling and J. Libuda, *J. Phys. Chem. C*, 2019, **123**, 31057–31072.
43 A. Nisters, T. Gutmann, S. M. Kim, J. P. Hofmann and M. Rose, *RSC Sustainability*, 2024, **2**, 2213–2217.
44 S. G. Guillet, I. Ibni Hashim, M. Beliš, K. Van Hecke, C. S. J. Cazin and S. P. Nolan, *Eur. J. Inorg. Chem.*, 2023, **26**, e202300327.
45 S. G. Guillet, G. Pisanò, S. Chakrabortty, B. H. Müller, J. G. de Vries, P. C. J. Kamer, C. S. J. Cazin and S. P. Nolan, *Eur. J. Inorg. Chem.*, 2021, **2021**, 3506–3511.
46 J. D. Scholten and J. Dupont, *Organometallics*, 2008, **27**, 4439–4442.
47 U. Hintermair, T. Gutel, A. M. Z. Slawin, D. J. Cole-Hamilton, C. C. Santini and Y. Chauvin, *J. Organomet. Chem.*, 2008, **693**, 2407–2414.
48 A. Bara-Estaún, C. L. Lyall, J. P. Lowe, P. G. Pringle, P. C. J. Kamer, R. Franke and U. Hintermair, *ChemCatChem*, 2023, **15**, e202201204.
49 M.-N. Birkholz (née Gensow), Z. Freixa and P. W. N. M. van Leeuwen, *Chem. Soc. Rev.*, 2009, **38**, 1099.
50 G. Petöcz, Z. Berente, T. Kégl and L. Kollár, *J. Organomet. Chem.*, 2004, **689**, 1188–1193.
51 A. J. Pontiggia, A. B. Chaplin and A. S. Weller, *J. Organomet. Chem.*, 2011, **696**, 2870–2876.
52 P. C. J. Kamer, P. W. N. M. van Leeuwen and J. N. H. Reek, *Acc. Chem. Res.*, 2001, **34**(11), 895–904.
53 G. L. Williams, C. M. Parks, C. R. Smith, H. Adams, A. Haynes, A. J. H. M. Meijer, G. J. Sunley and S. Gaemers, *Organometallics*, 2011, **30**, 6166–6179.
54 A. Buhling, P. C. J. Kamer, P. W. N. M. van Leeuwen, J. W. Elgersma, K. Goubitz and J. Fraanje, *Organometallics*, 1997, **16**, 3027–3037.
55 A. J. Sandee, L. A. van der Veen, J. N. H. Reek, P. C. J. Kamer, M. Lutz, A. L. Spek and P. W. N. M. van Leeuwen, *Angew. Chem., Int. Ed.*, 1999, **38**, 3231–3235.
56 G. M. Adams and A. S. Weller, *Coord. Chem. Rev.*, 2018, **355**, 150–172.
57 N. Mardirossian and M. Head-Gordon, *Mol. Phys.*, 2017, **115**, 2315–2372.
58 J. Arcau, M. Ferrer, E. Aguiló and L. Rodríguez, *Transition Met. Chem.*, 2017, **42**, 57–67.
59 F. Migliorini, E. Monciatti, G. Romagnoli, M. L. Parisi, J. Taubert, M. Vogt, R. Langer and E. Petricci, *ACS Catal.*, 2023, **13**, 2702–2714.
60 R. N. Wenzel, *Ind. Eng. Chem.*, 1936, **28**, 988–994.
61 S. Sunny, N. Vogel, C. Howell, T. L. Vu and J. Aizenberg, *Adv. Funct. Mater.*, 2014, **24**, 6658–6667.
62 D. Blaumeiser, R. Stepić, P. Wolf, C. R. Wick, M. Haumann, P. Wasserscheid, D. M. Smith, A.-S. S. Smith, T. Bauer and J. Libuda, *Catal. Sci. Technol.*, 2020, **10**, 252–262.
63 G. Kiedorf, D. M. Hoang, A. Müller, A. Jörke, J. Markert, H. Arellano-Garcia, A. Seidel-Morgenstern and C. Hamel, *Chem. Eng. Sci.*, 2014, **115**, 31–48.
64 E. Zuidema, L. Escorihuela, T. Eichelsheim, J. J. Carbó, C. Bo, P. C. J. Kamer and P. W. N. M. van Leeuwen, *Chem. – Eur. J.*, 2008, **14**, 1843–1853.